

Active operator learning with predictive uncertainty quantification for partial differential equations

Nick Winovich^{†a}, Mitchell Daneker^{†b,c}, Lu Lu^{*b}, Guang Lin^{*d,e,f}

^a*Sandia National Laboratories, Albuquerque NM, 87123*

^b*Department of Statistics and Data Science, Yale University, New Haven, CT 06511*

^c*Department of Chemical and Biomolecular Engineering University of Pennsylvania, Philadelphia PA, 19104*

^d*Department of Mathematics, Purdue University, West Lafayette IN, 47907*

^e*Department of Statistics, Purdue University, West Lafayette IN, 47907*

^f*Department of Mechanical Engineering, Purdue University, West Lafayette IN, 47907*

Abstract

In this work, we develop a method for uncertainty quantification in deep operator networks (DeepONets) using predictive uncertainty estimates calibrated to model errors observed during training. The uncertainty framework operates using a single network, in contrast to existing ensemble approaches, and introduces minimal overhead during training and inference. We also introduce an optimized implementation for DeepONet inference (reducing evaluation times by a factor of five) to provide models well-suited for real-time applications. We evaluate the uncertainty-equipped models on a series of partial differential equation (PDE) problems, and show that the model predictions are unbiased, non-skewed, and accurately reproduce solutions to the PDEs. To assess how well the models generalize, we evaluate the network predictions and uncertainty estimates on in-distribution and out-of-distribution test datasets. We find the predictive uncertainties accurately reflect the observed model errors over a range of problems with varying complexity; simpler out-of-distribution examples are assigned low uncertainty estimates, consistent with the observed errors, while more complex out-of-distribution examples are properly assigned higher uncertainties. We also provide a statistical analysis of the predictive uncertainties and verify that these estimates are well-aligned with the observed error distributions at the tail-end of training. Finally, we demonstrate how predictive uncertainties can be used within an active learning framework to yield improvements in accuracy and data-efficiency for outer-loop optimization procedures.

Keywords: [partial differential equations](#), [operator learning](#), [DeepONet](#), [uncertainty quantification](#), [out-of-distribution](#), [active learning](#)

1. Introduction

Understanding model uncertainty is critical for many data-driven methods; because of this, uncertainty quantification (UQ) has amassed a vast literature for quantifying what is known and what is unknown based on data availability [1–3]. When considering UQ in the context of machine learning and neural networks — which can universally approximate any continuous function [4–6] — applying traditional UQ techniques poses a challenge due to the complexity and black-box nature of the models. While accurate approximations can generally be obtained when sufficient training

[†]Equal contribution authors.

^{*}Corresponding authors. Email: lu.lu@yale.edu, guanglin@purdue.edu

data is available, the resulting model predictions are still approximations, and understanding the scale and nature of the model’s errors is essential for real-world applications.

Deep operator networks (DeepONets), introduced by Lu et al. [7] in 2019, are an emerging class of neural network models that target *operator* approximation instead of the more conventional function approximation. Operator networks are trained on a range of distinct problems so that the trained network embodies an operator that can be used to provide rapid approximations for a variety of different problem setups. By approximating operators, these models are capable of solving entire classes of problems with a single network, whereas conventional networks are designed to solve a single problem at a time. This class of network architectures has shown significant potential with regard to predictive power, generalizability, and robustness — as seen by the wide growth and application of DeepONets in recent years [8–26].

Given the prevalence of DeepONet models in practice, it is natural to ask whether such models can be enhanced to provide more information regarding the uncertainty and reliability of their predictions [20, 21, 21]. The work B-DeepONet [27] introduced a Bayesian training framework for quantifying uncertainties that result from noisy training data. This work demonstrated that the errors can be effectively quantified by incorporating probabilistic techniques into the calibration procedure for DeepONet models. While the focus of the present work does not involve noisy data, the results of B-DeepONet are promising as they show that DeepONet models can be augmented to provide accurate UQ predictions for certain problem formulations.

Yang et al. introduced UQDeepONet [28] to model uncertainty using randomized priors and leverages frequentist statistical techniques. Their work provides a scalable method for endowing DeepONets with uncertainty quantification in the presence of sufficient hardware resources, but adds significantly to the run-time costs when parallelization is not possible. This is due to the fact that the UQ framework is dependent on the evaluation of a full ensemble of independent networks; while this is generally acceptable during training, since the networks can be evaluated in parallel, it can be problematic for inference when computational resources are limited and predictions need to be made in real time.

We note that the works of Moya et al. [29, 30] were conducted in parallel with the work presented here. However, Moya’s work in 2022 focuses on applications and highlights the practical benefits of predictive uncertainty for real-time applications, demonstrating that the use of predictive uncertainty in place of ensemble Bayesian methods significantly reduces run-time costs while providing uncertainty estimates that align with Bayesian results. Moya’s 2025 work focuses on comparing conformalized DeepONets using predictive uncertainty and Bayesian ensemble uncertainty.

Pickering et al. [31] showed that DeepONet models equipped with UQ techniques can be used to improve active learning procedures. Active learning is framework for improving data efficiency of outer-loop analyses by leveraging uncertainty information to guide data acquisition. Since this can greatly reduce the costs and time spent collecting data, active learning plays an essential role in applications involving complex simulations or costly experiments [32–35]. The work of Pickering employed a Monte Carlo ensemble approach for uncertainty quantification, which was shown to outperform more conventional Gaussian process surrogates.

In this work, we investigate equipping DeepONet models with predictive uncertainty capabilities analogous to those provided by ConvPDE-UQ networks [36]. We train models to approximate the solution operators for a collection of linear and non-linear partial differential equations (PDEs). We place a particular emphasis on the statistical analysis of the predictive uncertainty estimates, and we assess the uncertainty framework’s generalization capabilities on in-distribution and out-of-distribution data. While the experiments conducted in this work involve PDEs on circular and rectangular domains, the framework and network implementations can also be applied on more general domains. Finally, to demonstrate a practical use-case for the predictive uncertainty framework,

we employ an uncertainty-equipped DeepONet model to accelerate an outer-loop optimization procedure using active learning. An overview of the uncertainty-equipped networks and active learning workflow is provided in Fig. 1. The main contributions of this work are summarized below.

- **Reliable uncertainty quantification in DeepONet.** Our predictive uncertainty framework provides reliable uncertainty estimates calibrated to the observed model errors.
- **Efficient uncertainty estimates.** The proposed framework’s predictive uncertainties provide accurate error estimates without reducing the accuracy or efficiency of DeepONet models.
- **Optimized DeepONet inference.** We introduce a computational method for DeepONet inference that significantly reduces run-time costs and enables use in real-time applications.
- **UQ-based active learning for accelerated convergence.** We demonstrate how predictive uncertainties can be leveraged to accelerate active learning with DeepONet surrogates. This enables active learning for problems involving *function-to-function* mappings, which are intractable for conventional approaches based on Gaussian process regression.

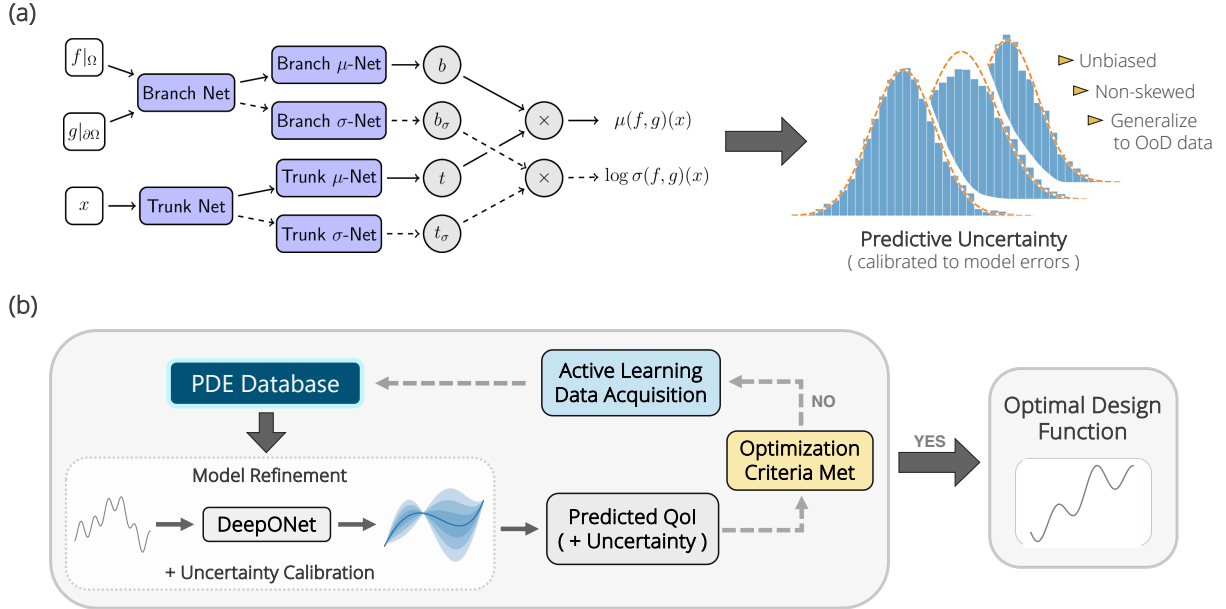


Figure 1: (a) The uncertainty-equipped operator network architecture splits predictions into mean and variance estimates. We interpret network outputs as parameters for a predictive probability distribution, which are calibrated to the observed error distributions during training. (b) The uncertainty estimates provided by the operator networks are employed to help guide outer-loop active learning procedures in *function spaces*. The quantity of interest (QoI) and variance estimates are derived from the operator network predictions, and this information is used to guide data acquisition by balancing exploitation and exploration.

The remainder of this paper is organized as follows. In Section 2.1, we provide background for the deep operator network architecture. This is followed by a detailed summary of the proposed predictive uncertainty framework in Section 2.2. We introduce an optimized computational workflow for DeepONet inference in Section 2.3 and describe the numerical sampling procedure for generating datasets in Section 2.4. We present the experimental results for several PDE problems in Section 3 along with a detailed analysis of the predicted uncertainty estimates. We demonstrate how these predictive uncertainties can be used to accelerate active learning procedures in Section 4, and provide concluding remarks and a discussion of future research directions in Section 5.

2. Uncertainty quantification in deep operator networks

2.1. Deep operator networks

DeepONet architectures are defined by two central components [7, 37, 38], referred to as the *branch network* and *trunk network*. The trunk network parses input coordinates corresponding to evaluation locations on the spatial (and/or temporal) domain $\Omega \subset \mathbb{R}^d$, and the branch network is responsible for processing information associated with the input functions, $(f, g) \in C(\Omega) \times C(\partial\Omega)$. The branch and trunk components produce vectors $b \in \mathbb{R}^N$ and $t \in \mathbb{R}^N$ with features extracted by the respective networks; these features are then combined to form the final network prediction, which is defined by the inner product $\hat{u}(f, g)(x) = \langle b, t \rangle$ for each location $x \in \bar{\Omega}$.

This predefined method of combining the outputs of the neural network components slightly restricts the expressivity of the resulting model, but it also provides a practical advantage with respect to interpretability. Since the output vector t of the trunk network depends solely on the input coordinates x , it is natural to interpret the components of the trunk output as functions defined on the underlying spatial domain of the PDE:

$$\text{Trunk}(x) = [\text{--- } t \text{ ---}] = [\varphi_1(x), \dots, \varphi_N(x)]$$

The component functions of the trunk network often bear a resemblance to the basis functions from finite element methods (FEM) [39, 40]. For DeepONet models, these basis functions are learned by the trunk network automatically during training, as opposed to being specified beforehand in the case of FEM calculations. The branch network assumes the role of determining the appropriate coefficients, b , for the family of basis functions proposed by the trunk. The resulting network approximation can then be expressed as

$$\hat{u}(f, g)(x) = \langle b, t \rangle = \sum_{i=1}^N b_i \cdot \varphi_i(x) \quad \text{where} \quad b = [b_1, \dots, b_N] = \text{Branch}(f, g).$$

This network prediction is evaluated by comparing it with the true PDE solution, $u(f, g)$, associated with the current input functions (f, g) , and the weights of the branch and trunk are updated to reduce discrepancies between the predicted and known solutions. More precisely, for a given input function pair $(f, g) \in C(\Omega) \times C(\partial\Omega)$, the DeepONet prediction $\hat{u}(f, g)$ is assigned a loss for each $x \in \bar{\Omega}$ given by

$$\text{Loss}(\hat{u}; x, f, g, u) = |\hat{u}(f, g)(x) - u(f, g)(x)|^2.$$

This loss is evaluated at randomly sampled locations on the interior and boundary of the domain to enforce both constraints of the target PDE. In contrast to function-approximation networks, the model is evaluated on a family of distinct input function pairs simultaneously during training. That is, the loss is averaged over spatial samples $x \in \bar{\Omega}$ and over function samples $(f, g) \in C(\Omega) \times C(\partial\Omega)$. This allows the model to approximate solutions to new realizations of input functions (f, g) after training, providing a surrogate model for the solution operator of the PDE.

2.2. Equipping operator networks with predictive uncertainties

In this section, we describe how DeepONet architectures can be extended to provide predictive uncertainties following a procedure analogous to that used in the ConvPDE-UQ framework [36, 41]. Under this framework, the model provides its predictions in the form of probability distributions instead of pointwise estimates. More precisely, the network is designed to produce parameter estimates for a class of distributions (such as the mean and standard deviation for a normal distribution). These parameters are calibrated during training to capture the distribution of observed errors; the resulting model then has the ability to provide uncertainty information along with its predictions.

To train DeepONets using this probability-based framework, we first need to select an appropriate parameterized family of probability distributions. In practice, this can be done by analyzing the empirical distribution of network errors observed during training. More precisely, a histogram of the observed network errors, such as the ones shown on the right of Fig. 2, can be compared with the density functions of common families of distributions, such as normal distributions.

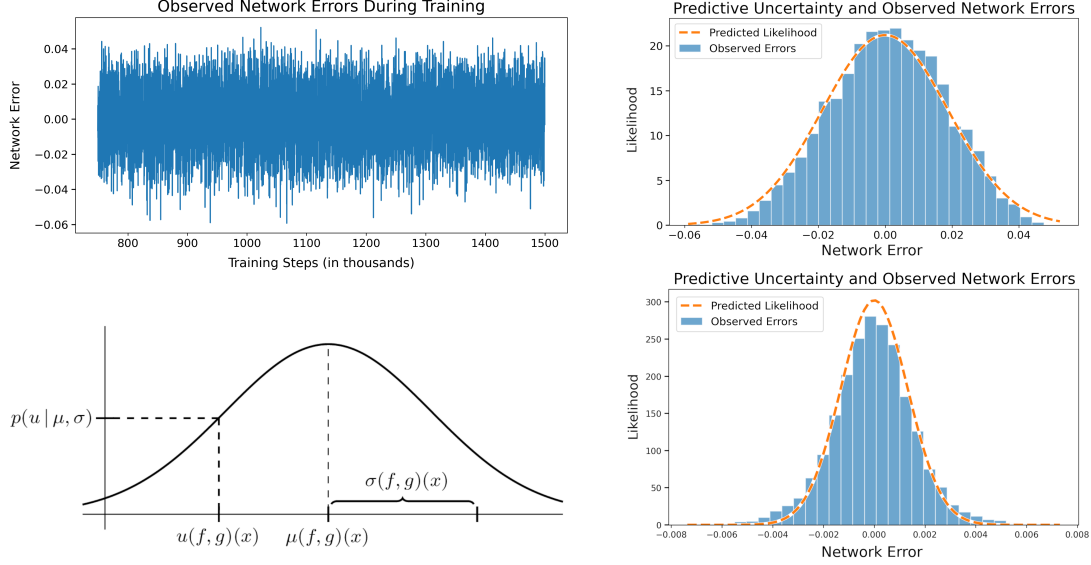


Figure 2: Observed network errors during training (top left) and interpretation of network outputs as parameters for a normal distribution (bottom left). The means and standard deviations provided by the network are used to assign likelihoods to the observed target values, and the network aims to increase these likelihoods during the training process. Histograms of the prediction errors for two input examples are shown to the right with predictive uncertainties overlaid to illustrate how the network uncertainty matches the observed errors near the end of training.

Once an appropriate family of parameterized probability distributions is selected, the network loss is defined with respect to the associated log likelihood function, following the analogy of Gaussian process regression used in the ConvPDE-UQ framework. For example, when the network errors are observed to follow a normal distribution, the model’s proposed likelihood for the true solution is $p(u; \mu, \sigma) = (2\pi\sigma^2)^{-1/2} \exp(-\frac{1}{2}|\mu(f, g)(x) - u(f, g)(x)|^2/\sigma^2)$, and the loss function is defined by:

$$\text{Loss}(\mu, \sigma; x, f, g, u) = \frac{1}{2}(\mu(f, g)(x) - u(f, g)(x))^2 / (\sigma(f, g)(x))^2 + \frac{1}{2} \log (2\pi(\sigma(f, g)(x))^2). \quad (1)$$

In this way, the network outputs $\mu(f, g)(x)$ and $\log \sigma(f, g)(x)$ ¹ are interpreted as parameters for a predictive probability distribution placed on the values of the true solution, as illustrated in Fig. 2.

After conducting experiments with several architecture variations (described in Appendix A.1), the network structure illustrated in Fig. 1(a) was found to provide the best performance. For the experiments presented in this work, the branch and trunk networks each consist of 5 fully-connected layers with 50 units and 30 units per layer, respectively. Each network layer uses Leaky ReLU activation functions [42], with the exception of the final layer of the branch network where no activation is applied. In order to equip the networks with predictive uncertainties, the final two layers of the branch and trunk are split to provide independent processing for the mean and uncertainty

¹To improve the stability of the numerical implementation, we interpret the uncertainty component of the network output on a logarithmic scale.

parameters. Specifically, two distinct pairs of 50 unit layers are used to produce the mean output b and uncertainty output b_σ of the branch network; similarly, two distinct pairs of 30 unit layers are used to produce the trunk outputs t and t_σ . The final network outputs for the distribution parameters are then defined by the inner products: $\mu(f, g) = \langle b, t \rangle$ and $\log \sigma(f, g) = \langle b_\sigma, t_\sigma \rangle$. For the experimental results presented in this work, the number of basis functions N was taken to be 150; however, the performance of the models remain essentially unchanged for any choice of $N > 50$.

2.3. Precomputation to decrease computational cost

When deploying DeepONet models for real-time applications, it is important to modify the computational workflow based on the target application. We consider two common use-cases where redundant calculations can be avoided to achieve significantly faster inference speeds. We first consider the construction of light-weight surrogate models for specific PDE solutions under the assumption of fixed input functions. This is followed by an overview of how inference can be performed efficiently on the full spatial domain for arbitrary input functions.

2.3.1. Precomputing branch weights

The first use-case we consider involves the construction of light-weight surrogate networks which can be used to approximate the solution function associated with fixed input data (f, g) . The optimization required for this type of application is simple, but yields a noticeable improvement in inference speed and helps motivate the more involved optimization steps introduced in Section 2.3.2.

In this setting, we note that the branch output b remains constant for any choice of evaluation location x , since the branch depends only on the fixed input data (f, g) . By precomputing the branch weights, the solution $\hat{u}(f, g)$ can be evaluated at arbitrary evaluation locations x using just a single forward-pass of the trunk network. In this context, the DeepONet framework can be seen as a natural generalization of the conventional function-approximator networks [43]; i.e., once the branch weights are fixed, the DeepONet framework yields fast neural network surrogates².

These light-weight surrogates also provide access to gradient information with very minimal overhead. In particular, since the branch output b is independent of the input coordinate x and the basis functions $\varphi_i(x)$ are defined by the neural network architecture of the trunk component, a linear differential operator \mathcal{L}_x can be applied to DeepONet surrogates by computing

$$\mathcal{L}_x[\hat{u}(f, g)(x)] = \mathcal{L}_x \left[\sum_{i=1}^N b_i \cdot \varphi_i(x) \right] = \sum_{i=1}^N b_i \cdot \mathcal{L}_x [\varphi_i(x)],$$

where $\mathcal{L}_x [\varphi_i(x)]$ is evaluated using automatic differentiation through the trunk network.

2.3.2. Precomputing trunk weights

A more common use-case for DeepONet models arises in applications where the input data (f, g) is expected to vary, and we are interested in evaluating solutions quickly at a fixed set of locations throughout the spatial domain. The optimization relevant for this form of inference is primarily based on precomputing the trunk weights. To achieve real-time speeds in practice, it is also necessary to make a few additional adjustments to the inference calculations.

To begin, we review the computational steps involved with evaluating a DeepONet model with input data (f, g) at a fixed set of evaluation locations $\{x_j\}_{j \in \mathcal{E}} \subset \overline{\Omega}$ with $|\mathcal{E}| = E$. First, we need to

²The key practical difference is that function-approximator networks need to be re-trained whenever the input data (f, g) is modified, while DeepONet surrogates can be obtained by simply recomputing the branch weights for the new inputs (requiring just one forward pass of the branch network).

evaluate the trunk at each of the input locations to form the matrix

$$T = \begin{bmatrix} \text{---} & t_1 & \text{---} \\ \vdots & \vdots & \vdots \\ \text{---} & t_E & \text{---} \end{bmatrix}, \quad \text{where} \quad t_j = [t_{j1}, \dots, t_{jN}] = \text{Trunk}(x_j).$$

The branch output vector is then computed for the current input data (f, g) , and the network prediction \hat{u} is given in vector form by

$$\begin{bmatrix} \hat{u}_1 \\ \vdots \\ \hat{u}_E \end{bmatrix} = \begin{bmatrix} \text{---} & t_1 & \text{---} \\ \vdots & \vdots & \vdots \\ \text{---} & t_E & \text{---} \end{bmatrix} \begin{bmatrix} b_1 \\ \vdots \\ b_N \end{bmatrix}, \quad \text{where} \quad b^T = [b_1, \dots, b_N] = \text{Branch}(f, g).$$

To interpret the vector prediction \hat{u} as a function on a two-dimensional domain, we must then place each of the entries $\hat{u}_j = \hat{u}(x_j)$ in a data structure which specifies the associated position x_j in the spatial domain. For example, it is often useful to have a discretized, two-dimensional representation of the predicted solution; to achieve this, we can specify evaluation locations $\{x_j\}_{j \in \mathcal{E}}$ based on a uniform $R \times R$ grid covering the domain and omit points that fall outside the domain. To efficiently convert the vector prediction into a structured array, we construct a sparse “placement matrix”, P , defined by mapping each index $j \in \mathcal{E}$ to the appropriate array location. More precisely, the placement matrix maps the j^{th} entry of the vector $\hat{u} \in \mathbb{R}^E$ to the column and row associated with position x_j in the two-dimensional matrix $\hat{U} \in \mathbb{R}^{R \times R}$ storing the structured prediction values.

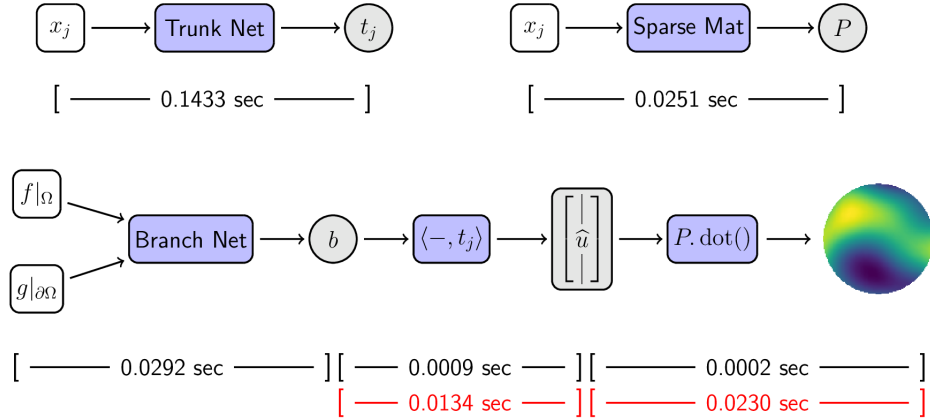


Figure 3: Inference is optimized for fast evaluations on a fixed grid by precomputing the trunk outputs for each grid location and constructing a sparse placement matrix to map vectorized network outputs to the correct array locations. The timings reported in the top row are one-time computations performed after training. Red timings denote unoptimized speeds using loops and manual entry placement, while black timings reflect the average runtime per input data pair (f, g) processed in batches. We note that the speedups reported use NumPy’s `einsum` operations applied to batched inputs and are not representative of single-example evaluations. The $\log \sigma$ calculation has been omitted from the diagram for brevity.

Inference can be performed naïvely by evaluating both the branch and trunk networks for every input pair (f, g) and evaluation location x , but doing so results in computation time ill-suited for real-time applications. By fixing evaluation locations and employing the inference strategy above, the inference time is significantly reduced. Once training is complete, the trunk outputs $\{t_j\}_{j \in \mathcal{E}}$ and placement matrix P only need to be computed once to facilitate inference for arbitrary input data (f, g) . With these one-time calculations in hand, the computation time for evaluating the DeepONet solution across the full domain can be reduced to approximately 0.029 seconds per problem (compared with 0.165 seconds when computed naïvely), as shown in Fig. 3.

2.4. Sampling procedure for randomized data generation

To construct the training datasets for the DeepONet models, we first employ Gaussian process sampling [44] to generate random realizations of the solution functions. In particular, we sample

$$u \sim \mathcal{G}(0, k_l(x, y))$$

from mean-zero Gaussian random fields with squared exponential covariance kernels $k_l(x, y) = \exp(-\|x - y\|^2 / 2l^2)$. Training data was generated using the length-scales $l \in \{0.2000, 0.2333, 0.2667, 0.3000\}$, and additional test data was generated for length-scales $l \in \{0.1333, 0.1667, 0.3333, 0.3667\}$. The test length-scales were intentionally selected outside of the range used to generate training data so that we can assess how well the proposed models generalize to out-of-distribution data.

The associated interior data $f \in C(\Omega)$ and boundary data $g \in C(\partial\Omega)$ are then computed by applying the forward differential operator and boundary operator directly to the sampled solution. This variation on the data generation allows us to construct training datasets without relying on conventional numerical solvers, such as FEM implementations; the datasets can be constructed whenever implementations of the forward differential operator and boundary operator are available.

The training data was initially generated on uniform spatial grids for simplicity, but this structured form of input data is not required for DeepONet models. To increase the complexity of the problems, we subsampled an unstructured set of *sensor locations* across the domain, $\{s_i\}_{i \in \mathcal{I}} \subset \Omega$, as illustrated on the right of Fig. 4. The branch network is provided data from the interior functions at these unstructured sensor locations (along with a complete vector of boundary data at locations $\{s'_j\}_{j \in \mathcal{J}} \subset \partial\Omega$). Training examples in the final dataset then take the form

$$(x, \{f(s_i)\}_{i \in \mathcal{I}}, \{g(s'_j)\}_{j \in \mathcal{J}}, u(f, g)(x))$$

with multiple evaluation locations $x \in \bar{\Omega}$ randomly sampled for each pair of input functions (f, g) . For the experiments in this work, we found it was sufficient to sample 50 evaluation locations per input function pair. We also conducted experiments with several different architectures for handling boundary data (as described in Appendix A.1), but found that simply appending boundary data to the branch network's input vector achieves the same performance as more structured approaches.

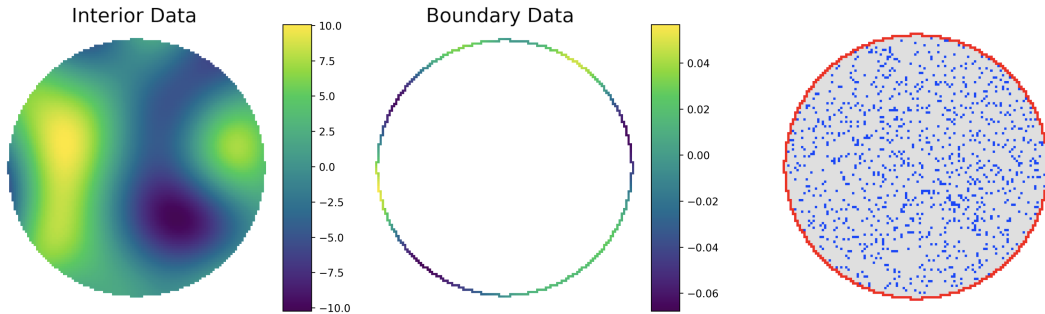


Figure 4: Example input data consisting of 2-dimensional interior data and 1-dimensional boundary data. DeepONet sensor locations for the interior data (blue) and boundary data (red) are shown on the right.

3. Validation of the proposed framework

While the proposed network architecture and training procedure allow DeepONet models to produce uncertainty estimates, it is important to verify these estimates are unbiased and generalize beyond the scope of the training data before employing these models in practice. In addition to assessing potential biases in the network predictions, it is natural to consider two distinct forms of generalization when evaluating the proposed training procedure:

1. Performance on unseen validation data sampled from length-scale classes used for training.
2. Performance on testing data sampled outside of the length-scale range seen by the network.

The first case corresponds to the network generalization on in-distribution data, while the latter corresponds to the generalization for out-of-distribution (OoD) data [45]. We first demonstrate that the network predictions are unbiased, and produce accurate predictions, on a set of linear problems. This is followed by a detailed analysis of the predictive uncertainty estimates. We then assess the network architecture’s generalization capabilities on two nonlinear problem setups.

The numerical results for the linear problems introduced in this section are summarized in Table 1, and results for the nonlinear setups are summarized in Table 2. The length-scales $\{0.2000, 0.2333, 0.2667, 0.3000\}$ correspond to the function spaces observed during training, while the length-scales $\{0.1333, 0.1667, 0.3333, 0.3667\}$ correspond to out-of-distribution data. We generated 5000 function realizations for each training length-scale (with 500 examples reserved for validation) along with 1000 realizations for each test length-scale. We note that in general, the DeepONet models are capable of achieving close to a 1% relative error for all problems, with performance worsening as the length-scale is reduced (as expected due to the increased data complexity in the low length-scale regime).

Poisson on Square with homogeneous BC								
l	0.1333	0.1667	0.2000	0.2333	0.2667	0.3000	0.3333	0.3337
MSE	4.78e-4	1.45e-4	5.17e-5	2.82e-5	2.10e-5	1.78e-5	1.60e-5	1.50e-5
MAE	1.71e-2	9.38e-3	5.60e-3	4.11e-3	3.51e-3	3.20e-3	3.01e-3	2.89e-3
L^1 Rel	3.33e-2	1.61e-2	8.60e-3	5.82e-3	4.62e-3	3.96e-3	3.63e-3	3.31e-3
L^2 Rel	3.19e-2	1.56e-2	8.36e-3	5.69e-3	4.55e-3	3.93e-3	3.62e-3	3.32e-3
Poisson on Square with inhomogeneous BC								
MSE	1.94e-2	4.17e-3	7.90e-4	1.67e-4	5.46e-5	3.22e-5	9.35e-5	8.83e-5
MAE	8.78e-2	3.80e-2	1.59e-2	7.21e-3	4.09e-3	2.95e-3	2.91e-3	2.63e-3
L^1 Rel	2.25e-1	9.87e-2	4.19e-2	1.92e-2	1.10e-2	8.04e-3	7.67e-3	6.91e-3
L^2 Rel	2.83e-1	1.32e-1	5.88e-2	2.76e-2	1.59e-2	1.15e-2	1.07e-2	9.66e-3
Poisson on Circle with inhomogeneous BC								
MSE	3.85e-3	5.23e-4	7.04e-5	1.43e-5	6.45e-6	3.08e-6	3.69e-6	3.66e-6
MAE	4.63e-2	1.66e-2	6.07e-3	2.70e-3	1.63e-3	1.22e-3	1.07e-3	9.37e-4
L^1 Rel	1.20e-1	4.40e-2	1.64e-2	7.43e-3	4.51e-3	3.42e-3	3.06e-3	2.60e-3
L^2 Rel	1.28e-1	4.79e-2	1.83e-2	8.30e-3	4.97e-3	3.75e-3	3.35e-3	2.86e-3

Table 1: Numerical results for the linear problem setups across each length-scale class. Mean squared errors (MSE), mean average errors (MAE), and L^1/L^2 relative errors are reported for each length scale, shown in columns.

3.1. Poisson Equations with Homogeneous and Inhomogeneous BCs

The first problem we consider is the Poisson equation on a square domain with homogeneous boundary conditions, as described by Eq. (2a). This is a simple problem, and if the proposed model performs poorly in this setting, we can conclude that the proposed addition of UQ is negatively impacting accuracy. Overall, the network predictions for this problem setup are accurate, as shown in Table 1, with relative errors below 1%. This allows us to move on to more complex problems with confidence that the UQ framework is not undermining the accuracy of network predictions.

$$\begin{cases} \Delta u = f & \text{in } \Omega \\ u = 0 & \text{on } \partial\Omega \end{cases} \quad (2a) \qquad \begin{cases} \Delta u = f & \text{in } \Omega \\ u = g & \text{on } \partial\Omega \end{cases} \quad (2b)$$

We next consider the Poisson equation with inhomogeneous boundary conditions in Eq. (2b) for both a square and circular domain. The errors are comparable for the square and circular domains, but overall the circular domain yields lower errors than the square domain. This difference is depicted in Table 1, and a qualitative assessment of the network results is provided in Fig. 5. As an initial assessment of the predictive uncertainties, we note that the percentages of the dataset where errors exceed the predicted standard deviations align well with the empirical 68-95-99.7 rule for normally distributed data. This suggests the predictive uncertainty may capture the model errors correctly and motivates a more thorough analysis of the uncertainty results.

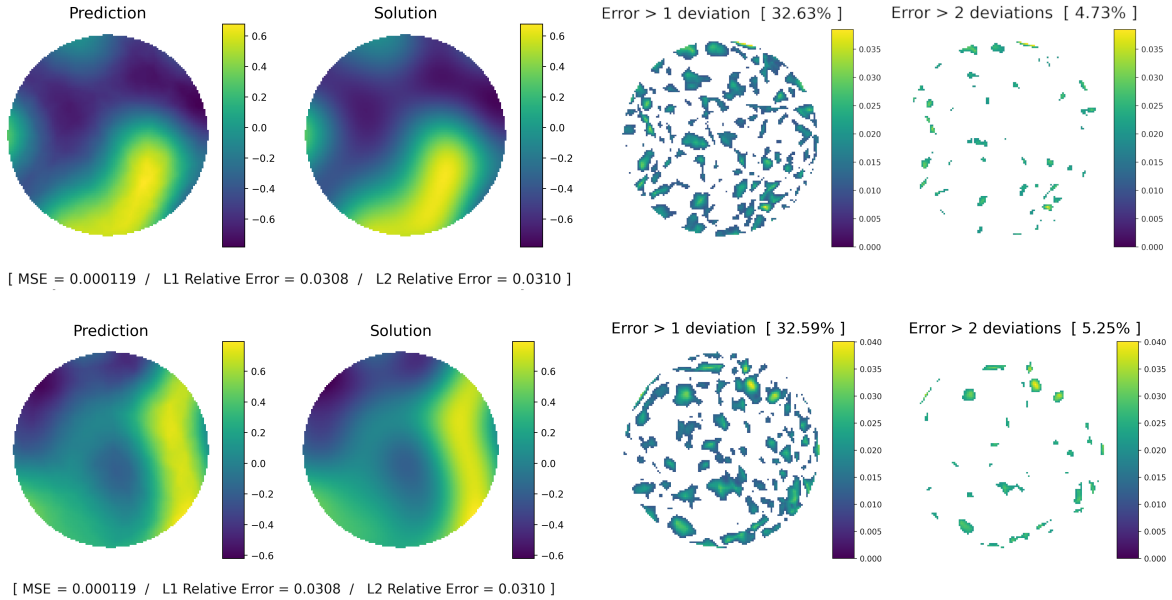


Figure 5: Qualitative results for two examples of the Inhomogeneous Poisson setup show that predictions provide accurate approximations to the true solutions. The network’s predictive uncertainty closely matches the empirical 68-95-99.7 rule, with around 32% of the observed errors above 1 standard deviation and around 5% above 2 deviations.

3.2. Assessment of predictive uncertainty framework

To evaluate the proposed uncertainty framework, we assess the model predictions for 500 validation examples on the circular domain for the inhomogeneous Poisson equation. We evaluate the predicted uncertainties with respect to the distribution of observed model errors (see Fig. 2), and assess the overall distribution of predicted uncertainties compared with the observed standard

Nonlinear Poisson with inhomogeneous BC								
l	0.1333	0.1667	0.2000	0.2333	0.2667	0.3000	0.3333	0.3337
MSE	4.46e-3	4.79e-4	6.71e-5	1.64e-5	9.30e-6	5.92e-6	1.97e-5	1.70e-5
MAE	4.95e-2	1.67e-2	6.24e-3	3.01e-3	2.00e-3	1.58e-3	1.54e-3	1.41e-3
L^1 Rel	1.29e-1	4.43e-2	1.67e-2	8.07e-3	5.31e-3	4.21e-3	3.94e-3	3.66e-3
L^2 Rel	1.32e-1	4.61e-2	1.77e-2	8.58e-3	5.64e-3	4.48e-3	4.20e-3	3.89e-3
Diffusion-Reaction with inhomogeneous BC								
MSE	6.87e-3	1.28e-3	2.70e-4	8.83e-5	6.65e-5	5.77e-5	4.87e-5	5.67e-5
MAE	6.50e-2	2.77e-2	1.22e-2	6.48e-3	4.57e-3	3.89e-3	3.61e-3	3.51e-3
L^1 Rel	1.69e-1	7.27e-2	3.24e-2	1.69e-2	1.17e-2	9.85e-3	9.26e-3	8.97e-3
L^2 Rel	1.71e-1	7.47e-2	3.37e-2	1.77e-2	1.23e-2	1.04e-2	9.84e-3	9.55e-3

Table 2: Numerical results for the nonlinear problem setups across each length-scale class.

deviations in the network errors at the tail-end of training. We also analyze the bias, skew, and kurtosis of the distributions of observed errors for each of the 500 validation examples. This analysis is used to verify that normal distributions are suitable candidates for modeling the observed error; histograms summarizing these results are provided in Fig. 6.

The biases of the error distributions at the tail-end of training are consistently small, with values ranging from -0.0018 to 0.0019 . The histogram of biases is also symmetric and roughly centered at zero, indicating that the network does not have any tendency to over-estimate or under-estimate function values consistently across the dataset. The skew values for the observed error distributions are also approximately symmetric and centered at zero, with a minimum skew of -0.4739 and maximum skew of 0.3715 . The majority of error distributions have skews with magnitudes below 0.2 , indicating the distributions are roughly symmetric. Since we elected to use normal distributions to model uncertainty, it is important to verify the observed error distributions are sufficiently symmetric. If the observed errors have skewed distributions, the loss function in Eq. (1) can be replaced with the negative log-likelihood for a different class of distributions (see Appendix B of [36]).

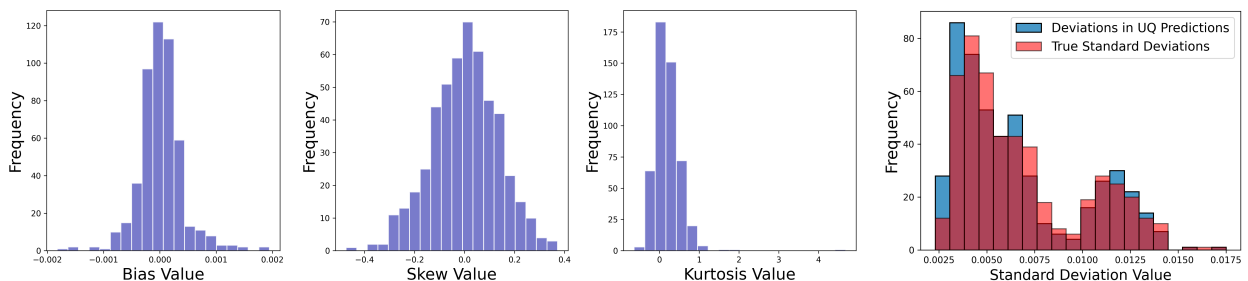


Figure 6: Biases (left), skews (center-left), and kurtosis (center-right) of the observed error distributions at the tail-end of training for 500 validation examples from the Inhomogeneous Poisson equation over a circular domain. To the right, we show the observed standard deviations in errors at the end of training (blue) and the network’s predicted uncertainties (pink) for 500 examples from the Inhomogeneous Poisson; the significant overlap (maroon) provides evidence that the network uncertainty is accurately capturing the model errors.

A similar analysis of the kurtosis of the observed errors shows a generally positive and skewed right distribution. Kurtosis measures the “tailedness” of a distribution, with a higher value indicating more outliers [46]. Most of the kurtosis values are close to zero with a slight bias in the positive direction. While this means they will generally have slightly longer tails and sharper peaks, all

kurtosis values are well within the standard reference interval, $[-2, 2]$, for a normal distribution.

Finally, we consider how the predicted errors stand up to the true errors. The network provides standard deviation estimates which we compare with the true standard deviations of the error distributions observed at the tail-end of training. We evaluated the predicted and true standard deviations across 500 validation examples and found the average relative error to be 0.0718. The histogram on the right of Fig. 6 shows how the distribution of predicted uncertainties compares with the observed standard deviations. There is a considerable overlap between the histograms (shown in maroon), and we see that the overall distribution is accurately captured by the UQ procedure. This provides evidence that the predictive uncertainty framework is operating correctly and can accurately predict the variance in the network predictions. Our assessments of the predictive uncertainty for the other problem setups were consistent with the analysis presented above.

3.3. Nonlinear Poisson Equation and Diffusion-Reaction Equation

Nonlinearity adds additional complexity in traditional solvers and provides a more challenging benchmark for evaluating DeepONet models. For our first nonlinear problem setup, we consider the nonlinear Poisson formulation described in Eq. (3a). A summary of the network prediction errors across different length-scales is provided in Table 2. The predictions for this setup are also accurate, with errors comparable to the linear setups, and examples of the DeepONet predictions are shown in Fig. 7. We see that the predictions accurately approximate the true solutions and yield noisy, unstructured error profiles with maximum values on the same order as the predictive uncertainties.

$$\begin{cases} \operatorname{div}((1+u^2)\nabla u) = f & \text{in } \Omega \\ u = g & \text{on } \partial\Omega \end{cases} \quad (3a) \quad \begin{cases} \Delta u + u^2 = f & \text{in } \Omega \\ u = g & \text{on } \partial\Omega \end{cases} \quad (3b)$$

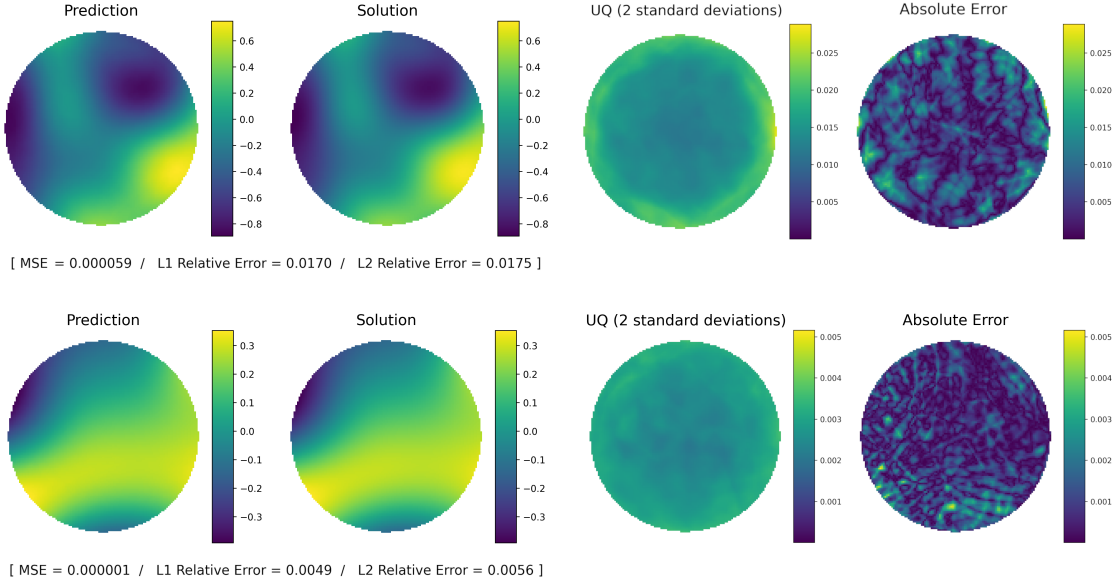


Figure 7: DeepONet results on validation dataset for Nonlinear Poisson equation on unit circle with predicted and true solutions shown on left. The observed error profiles (right) are seen to be unstructured and resemble random noise. The network’s predictive uncertainty is relatively flat across the domain and accurately captures the scale of the network errors. While the predictive uncertainty does not capture the precise locations of errors, the percentages falling within the uncertainty bounds still align well with the empirical rule, similar to the results shown in Fig. 5.

The final problem setup we consider is a nonlinear diffusion-reaction prescribed by Eq. (3b). A summary of the accuracies of the DeepONet model for each length-scale is provided in Table 2. Overall, the prediction errors are slightly higher than those encountered in previous setups, likely stemming from the increased complexity of the system. We also note that the larger relative errors are more pronounced in the smaller length-scales, especially the length-scales 0.1333 and 0.1667, which were withheld during training. Since the errors are higher for this setup, it is natural to ask whether the predictive uncertainty correctly reflects the change in accuracy. Ideally, we would also like the uncertainties to provide an indication of the drop in performance at lower length-scales.

3.4. Generalization to Out-of-Distribution Data

To assess the proposed uncertainty framework’s generalization capabilities, we evaluate the model’s performance on unseen in-distribution and out-of-distribution data. In the presence of sufficient training data, the prediction accuracy of the DeepONet models on in-distribution validation data matches the accuracy on training examples across all length-scales. The associated uncertainty estimates are also well-calibrated to the validation errors when sufficient training data is available, as shown in Fig. 8.

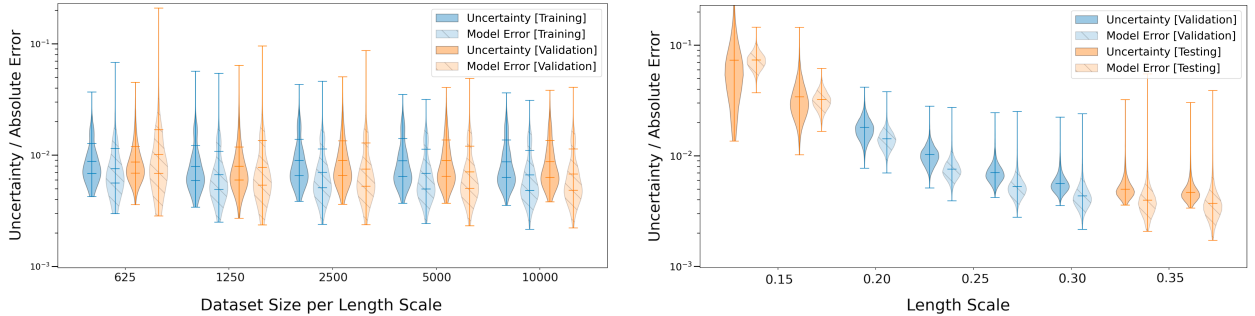


Figure 8: Comparison of DeepONet performance on training and validation examples for different training dataset sizes for the Nonlinear Diffusion-Reaction problem setup (left). The network converges well even with limited training data, but the performance is also observed to level off quickly as the number of training examples increased indicating data saturation and a possible limit to the network’s accuracy. To the right, we provide an analysis of predictive uncertainty produced by a DeepONet model on the Nonlinear Diffusion-Reaction problem setup. When evaluated on in-distribution validation data (blue) as well as out-of-distribution test data (orange) the network’s uncertainty is seen to accurately capture the observed model error.

Of greater interest is the fact that the predictive uncertainties generalize quite well to out-of-distribution data, as shown in the second plot of Fig. 8. As noted earlier, the lower length-scale classes correspond to more difficult problems; accordingly, the network performance gradually decays as the length-scale is reduced. Notably, the predictive uncertainties for the smallest length-scales are also observed to increase, reflecting the rising network errors associated with the out-of-distribution data. However, this rise in uncertainty does not occur for the out-of-distribution at the other extreme (i.e., length-scales larger than those seen during training), which correctly reflects the model performance for these simpler problems.

This shows that the network can, to some extent, automatically determine the difficulty associated with a given problem. More precisely, the accuracy of the network’s predictive uncertainties extends beyond the scope of the function classes observed during training. The network is never provided any labeling information regarding the length-scale values, so the network’s predictive uncertainty is based solely on features extracted from the raw input function values.

4. Accelerating active learning with predictive uncertainties

In this section, we demonstrate how the proposed uncertainty framework can be used to accelerate outer-loop active learning procedures. We consider a system of time-dependent functions parameterized by a vector $\theta = (\alpha, \beta)$ with $\alpha \in [-7, 4]$ and $\beta \in [0, 6]$. The system consists of an acceleration $f_\theta(t)$, velocity $u_\theta(t)$, and final position q_θ defined by

$$\begin{aligned} f_\theta(t) &= -(1 + \alpha) \cdot \alpha \cdot \sin(\alpha t) - \cos^2(\beta) \cdot e^{t \cos(\beta)}, \\ u_\theta(t) &= (1 + \alpha) \cdot \cos(\alpha t) - \cos(\beta) \cdot e^{t \cos(\beta)}, \\ q_\theta &= \int_0^1 u_\theta(t) dt = \frac{1 + \alpha}{\alpha} \sin(\alpha) - e^{\cos(\beta)}. \end{aligned}$$

Our goal is to identify the parameters $\theta = (\alpha, \beta)$, along with the corresponding velocity function $u_\theta(t)$, that maximize the final position of the system, q_θ . We consider two formulations of this problem, with both leveraging DeepONet models to approximate the system’s velocity function based on acceleration information. In the first formulation, we provide the DeepONet model with the underlying system parameters (α, β) as input; we refer to this as the *parameter-to-function* setup. For the second formulation, we provide the model with time-series data containing acceleration information; we refer to this as the *function-to-function* setup. In both cases, the network is trained to predict the velocity function $u_\theta(t)$, along with the associated uncertainty estimates. We then derive the quantity of interest (QoI) from the predicted velocity using the quadrature rule

$$\hat{q}_\theta = \int_0^1 \hat{u}(t) dt \approx \frac{1}{2n} \left(\hat{u}(t_0) + \hat{u}(t_n) + 2 \sum_{i=1}^{n-1} \hat{u}(t_i) \right)$$

This quadrature rule is also applied to the predictive uncertainties in the velocity function, allowing us to derive an implied uncertainty, $\sigma(\hat{q}_\theta)$, on the quantity of interest \hat{q}_θ .

We will identify the optimal velocity function using as few system queries as possible; this is a common requirement for practical applications where data collection is expensive and/or time-consuming and QoI estimates must be made using a limited budget of system interrogations. For improved data efficiency, we employ active learning to iteratively refine the DeepONet model and direct our search for the optimal system configuration. The governing equations for this problem were specifically designed to include two peaks inside the constrained parameter space: a local maximum at $(-4.7680, \pi)$ and a global maximum at $(1.2150, \pi)$, as shown in Fig. 9. We start with a random selection of points with $\alpha < -2.0$, so that the initial observations are confined to the left half of the domain with a bias toward the local maximum.

The proposed active learning procedure leverages the uncertainty estimates of the DeepONet models to *explore* the parameter space in regions of high uncertainty while also *exploiting* the mean predictions to search regions with high predicted QoI values. To assess the performance of the active learning procedure, we compare its results with greedy (exploitation-driven) and random (exploration-driven) alternatives. Details for the three strategies are summarized below:

- **Active Learning with UQ:** New query locations are proposed based on the upper confidence bound induced by the network’s predictive uncertainty. We evaluate the network on a grid of parameter values, $\Lambda \subset [-7, 4] \times [0, 6]$, and integrate the network’s velocity predictions to obtain mean and standard deviation estimates for the QoI. We use the acquisition values $\hat{q}_\theta + \varepsilon \cdot \sigma(\hat{q}_\theta)$ to rank the query locations $\theta \in \Lambda$, where $\varepsilon > 0$ is used to weight the impact of uncertainty. The system is then evaluated at the locations with the highest acquisition values, and the network is re-trained with the augmented dataset before the next active learning iteration.

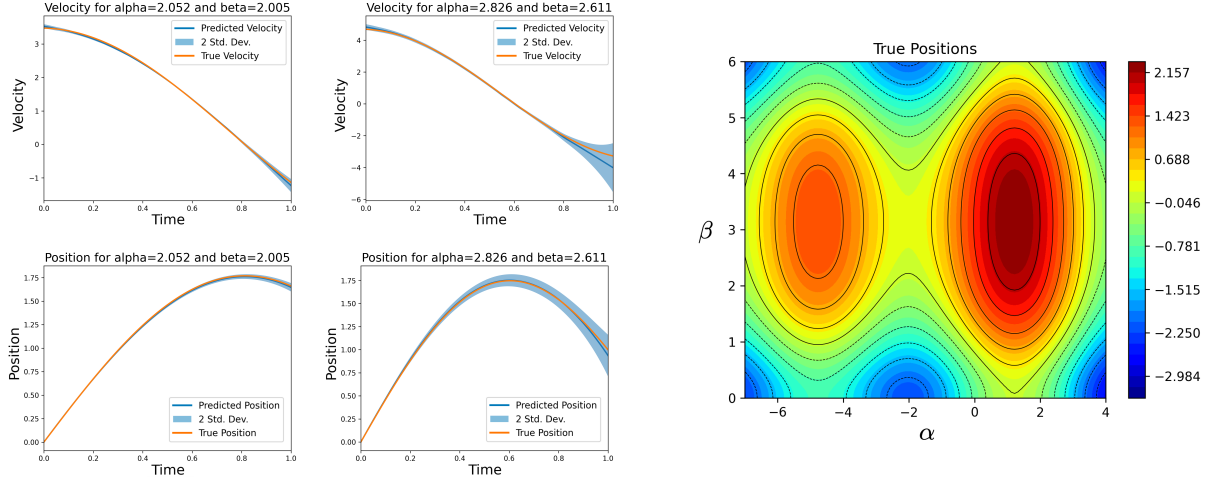


Figure 9: Example trajectories for velocity (upper-left) and position (lower-left) along with network predictions at the end of function-to-function learning. The true position field at time $t = 1$ is plotted on the right for parameter values $\alpha \in [-7, 4]$ and $\beta \in [0, 6]$. The position field contains two peaks: a local maximum on the left and a global maximum on the right. We sample the initial training locations around the local maximum to assess the framework’s ability to avoid local trapping.

- **Greedy:** We train a standard DeepONet model, without uncertainty, to approximate the velocity functions and integrate the predictions to obtain QoI estimates. We select the parameters $\theta \in \Lambda$ with the highest predicted QoI values, \hat{q}_θ , and perform additional system queries at these locations. The network is then re-trained before starting the next iteration.
- **Random:** We train an uncertainty-equipped DeepONet model using query locations sampled uniformly from the parameter grid Λ at each iteration.

For both the active learning and greedy strategies, a degree of random exploration is introduced to balance exploitation and exploration. During the initial iterations, we supplement the model’s proposed query locations with additional points sampled uniformly from the parameter grid Λ . We found this significantly improved the consistency of both approaches and helped prevent instances of local trapping³.

4.1. Parameter-to-Function Learning

In the first formulation, we feed the parameters (α, β) directly into the branch network of the DeepONet and train the trunk network using randomly sampled time locations on the interval $[0, 1]$. An initial training dataset is created by randomly sampling 50 parameter locations in $[-7, -2] \times [0, 6]$ and computing the associated velocity functions. The DeepONet model is tasked with approximating the mapping $\theta \mapsto u_\theta(t)$, and we use the predictive uncertainty estimates to compute the value of the upper confidence bound acquisition function [47]. This acquisition function is used to select the next batch of queries for each active learning iteration. To obtain batches of distinct query locations, we define a selection distance, $\delta_\tau > 0$, that specifies the minimum allowable distance between queries proposed at the current iteration, τ . We achieve this by selecting query locations

³Both the active and greedy strategies occasionally converged to the local maximum during our initial experiments. This problem was resolved by incorporating random exploration to supplement both search strategies.

sequentially according to the following rule:

$$\theta_{\tau,k}^* = \operatorname{argmax}_{\theta \in \Lambda_{\tau,k}} \hat{q}_\theta + \varepsilon_\tau \cdot \sigma(\hat{q}_\theta), \quad \text{where} \quad \Lambda_{\tau,k} = \{\theta \in \Lambda : |\theta - \theta_{\tau,j}^*| > \delta_\tau \ \forall j < k\}. \quad (4)$$

We gradually decay the values of the exploration weight, ε_τ , and selection distance, δ_τ , by setting $\varepsilon_\tau = 2 \cdot (0.9)^\tau$ and $\delta_\tau = 1 \cdot (0.9)^\tau$. This allows the model to propose more precise (and greedier) query locations in later iterations to refine its final prediction for the optimal parameters.

At each learning iteration, we evaluate the system at 10 query locations selected using Eq. (4) for the active setup, the highest predicted QoI for the greedy strategy, and uniformly sampled locations for the random approach. To assist with exploration, we also include 5 randomly sampled query locations during the initial iteration. We reduce the number of random points added by a factor of 0.9 for subsequent iterations, rounding decimal values to the nearest integer. We perform 20 learning iterations for each strategy, resulting in a total of 294 system queries. We conducted 50 independent trials for each strategy to assess performance across different initial sample locations. The initial data locations were sampled randomly for each of the 50 trials, and each learning strategy used the same initial samples to provide a fair comparison of the results.

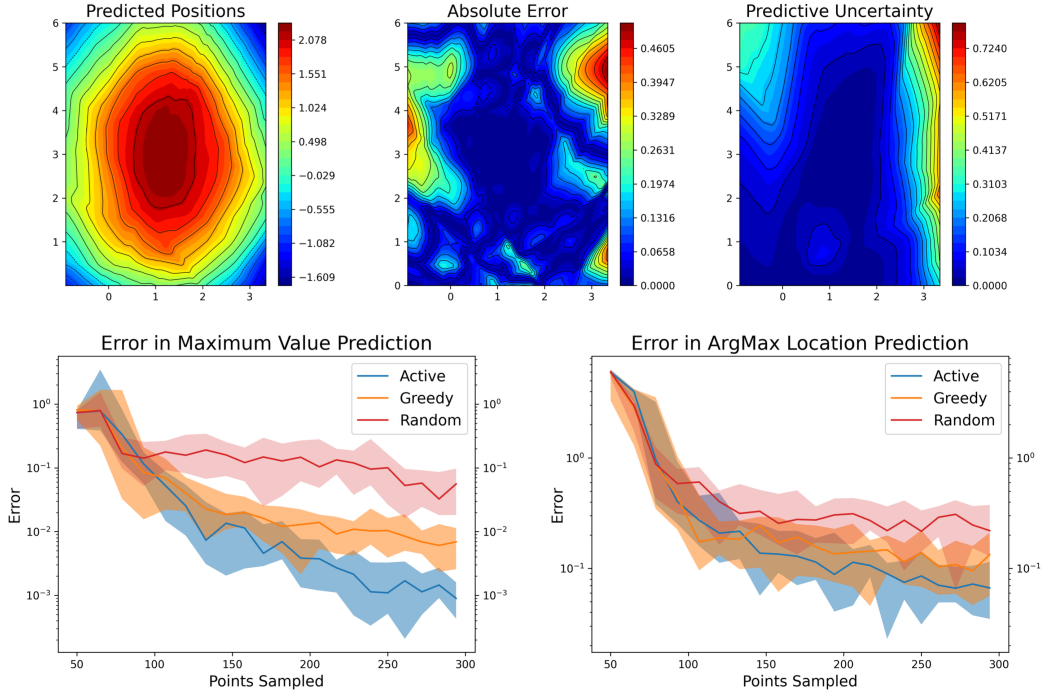


Figure 10: Results for parameter-to-function active learning problem. Plots of the final predicted position field at time $t = 1$ (top left), the absolute error relative to the ground truth (top center), and the model’s predicted uncertainty in position (top right). By construction of the active learning setup, the model is most accurate near the peak location, $(1.2150, \pi)$. The uncertainty in position is derived from the model’s UQ predictions for velocity and give a reasonable approximation of the observed errors. We conducted 50 trials for each learning strategy, with each trial consisting of 20 active learning iterations. The median and spread between the 0.2-quantile and 0.8-quantile are plotted (bottom) for each iteration to summarize the results across trials. The errors in the predicted maximum function value are shown on the left, and errors in the predicted maximal location are shown to the right.

Examples of ground-truth and predicted velocity functions are shown in Fig. 9, along with the network’s predicted uncertainty bounds. These mean and uncertainty functions are integrated over time to obtain estimates for the final position (and uncertainty in position). A qualitative summary of the position predictions produced by the active learning procedure are shown in Fig. 10.

We note that the error is lowest in a neighborhood around the global peak, indicating the active learning procedure correctly targeted this region for refinement. The uncertainty estimates also align relatively well with the observed errors; however, the network uncertainty underestimates errors in the region $\alpha < 0$, possibly due to the limited amount of training data available.

We assess the performance of each learning strategy using two metrics: the error in the predicted maximum QoI value and the error in the maximizing parameters for the QoI. The ground truth solution for the maximum value is $q_{\theta^*} \approx 1.3410$, which occurs at $\theta^* = (1.2150, \pi)$. A quantitative comparison between the active, greedy, and random strategies is provided in Fig. 10, which summarizes the results from 50 trials of each learning strategy. The uncertainty-equipped DeepONet model achieves the lowest errors in both the maximum value and maximizing parameter estimates. For the maximum value metric, the active setup achieves a median final error of $8.96\text{e-}4$ over 50 trials, while the greedy and random strategies had median errors of $6.90\text{e-}3$ and $5.59\text{e-}2$, respectively. The performance difference for parameter estimation was less pronounced, but the active setup still achieved the lowest median error, 0.067 , compared with median errors of 0.133 and 0.219 for the greedy and random approaches.

4.2. Function-to-Function Learning

For the second experiment, we modify the branch input of the DeepONet to use time-series observations of acceleration instead of the parameters α and β . We create an initial training dataset by randomly sampling 10 parameter locations in the interval $[-7, -2] \times [0, 6]$ and computing the associated acceleration and velocity functions. The DeepONet model is then tasked with predicting velocity functions based on time-series information regarding acceleration.

Initial experiments showed the direct function-to-function mapping was too simple to benefit from active learning. The mapping from acceleration to velocity amounts to a straight-forward integral estimate, and the models provided accurate approximations with minimal system interrogations. To increase the problem complexity, we modify the acceleration information passed to the network using the following transformation:

$$f_{\theta}^{\text{input}}(t) = \left(1 + \exp\left(-\frac{1}{2}f_{\theta}(t)\right)\right)^{-1} - \frac{1}{2}.$$

We compute the modified acceleration values at 33 temporal locations on the interval $[0, 1]$, and use these values as the function inputs to the network. Since the velocity function has an initial value that is independent of acceleration, we assume the initial velocity, $u_{\theta}(0) = 1 + \alpha - \cos(\beta)$, is known for each parameter θ . We then sum the known initial velocity with the network’s output before computing the network’s loss relative to the true velocity function.

At each learning iteration, we evaluate the system at 5 query locations proposed by each learning strategy. We also include 4 randomly sampled query locations during the initial iteration, and we reduce the number of random points added by a factor of 0.9 for subsequent iterations. We perform 20 learning iterations for each strategy, resulting in a total of 152 system queries. We conducted 50 independent trials for each strategy using the same initialization procedure as before.

A qualitative summary of the position predictions for the function-to-function setup are shown in Fig. 11. We note that the predicted positions are more accurate, and better structured, than those obtained in the parameter-to-function setup (which had access to nearly twice as many system interrogations). The predicted uncertainty also aligns well with the observed errors, although it still underestimates errors in some regions (likely due to the limited data available).

We assess the performance of each learning strategy using the same metrics as the parameter-to-function setup, and we again find that active learning with the uncertainty-equipped DeepONet model outperforms the greedy and random alternatives. A quantitative comparison of each strategy’s performance over 50 trials is provided in Fig. 11. For the maximum value metric, the active

setup achieves a median final error of $2.27\text{e-}4$ over 50 trials, while the greedy and random strategies had median errors of $1.50\text{e-}3$ and $1.25\text{e-}2$, respectively. For the maximizing parameter estimates, the active setup achieved the lowest median error, $3.69\text{e-}3$, compared with median errors of $7.51\text{e-}3$ and $3.11\text{e-}2$ for the greedy and random approaches.

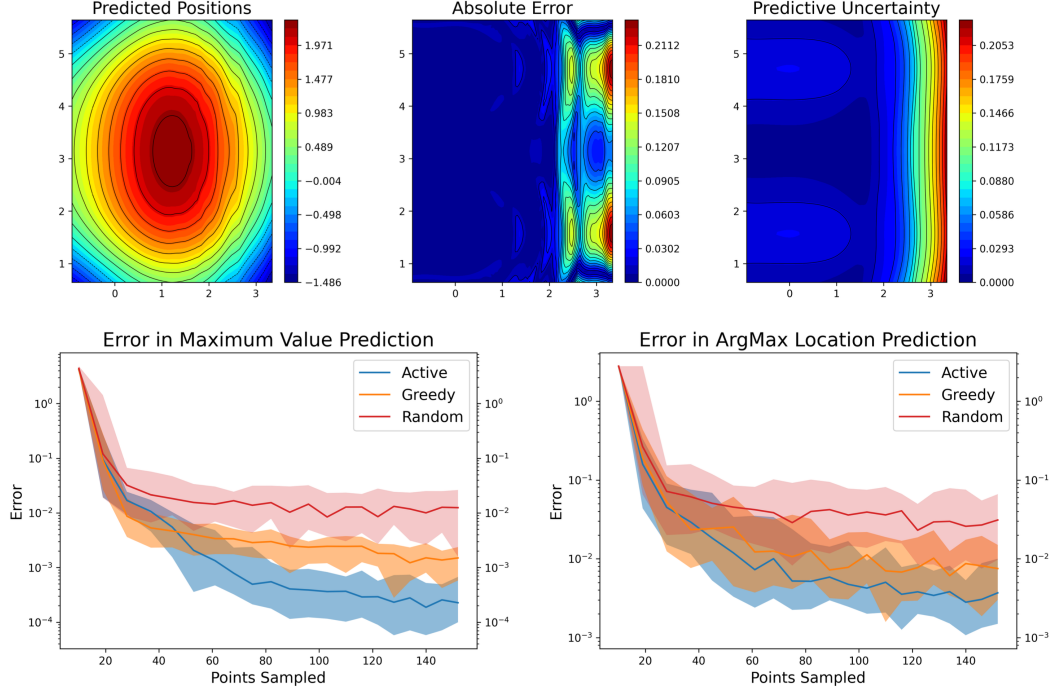


Figure 11: Results for function-to-function active learning problem. The final predicted position field at time $t = 1$ for the function-to-function setup (top left). The predicted positions accurately reflect the ground truth values everywhere except the far-right side of the domain, as seen in the plot of observed errors (top center), which is consistent with the predicted uncertainty (top right). We conducted 50 trials for each learning strategy, with each trial consisting of 20 active learning iterations. The median and spread between the 0.2-quantile and 0.8-quantile are plotted for each iteration to summarize the results across trials. The error in the predicted optimal value (bottom left) and predicted optimal location (bottom right) are plotted for each learning strategy. The active learning strategy enabled by predictive uncertainty estimates yields an order of magnitude improvement in optimal value prediction.

5. Conclusions

In this work, we conducted a series of experiments investigating a light-weight uncertainty quantification framework for deep operator networks. We trained models using a log-likelihood loss function to calibrate predictive uncertainty estimates to the errors observed at the tail-end of training. We evaluated the models on a variety of linear and non-linear PDE problems and explored several architecture variants to identify the best configurations for incorporating boundary conditions and uncertainty estimates. We also introduced an optimized computational graph that yields an order-of-magnitude reduction in evaluation time and enables fast operator inference for real-time applications. We presented a detailed statistical analysis of the UQ framework and verified that the predictive uncertainties accurately reflect the observed error distributions. We showed the uncertainty estimates also generalize well to out-of-distribution data by evaluating the models on function spaces unseen during training.

Finally, we demonstrated how the uncertainty-equipped operator networks can be used to accelerate outer-loop active learning procedures. This resulted in nearly an order-of-magnitude improvement over standard DeepONet models. The active learning results presented in this work were conducted using simple, proof-of-concept systems. In future research, we plan to provide a more comprehensive analysis of how uncertainty-equipped operator networks can be leveraged in the context of outer-loop active learning procedures.

Acknowledgments This paper describes objective technical results and analysis. Any subjective views or opinions that might be expressed in the paper do not necessarily represent the views of the U.S. Department of Energy or the United States Government. Sandia National Laboratories is a multimission laboratory managed and operated by National Technology and Engineering Solutions of Sandia LLC, a wholly owned subsidiary of Honeywell International, Inc., for the U.S. Department of Energy’s National Nuclear Security Administration under contract DE-NA-0003525 (SAND2025-02567O). GL would like to thank the support of National Science Foundation (DMS-2053746, DMS-2134209, ECCS-2328241, CBET-2347401 and OAC-2311848), and U.S. Department of Energy (DOE) Office of Science Advanced Scientific Computing Research program DE-SC0023161, the Uncertainty Quantification for Multifidelity Operator Learning (MOLUcQ) project (Project No. 81739), and DOE–Fusion Energy Science, under grant number: DE-SC0024583. LL was supported by the U.S. DOE Office of Advanced Scientific Computing Research under Grants No. DE-SC0025593 and No. DE-SC0025592 and the U.S. National Science Foundation under Grant No. DMS-2347833.

Appendix A. Implementation details

DeepONet models can be equipped with predictive uncertainties by (1) selecting a parameterized family of distributions, (2) extending the network outputs to provide estimates for each parameter, and (3) defining a loss function based on the negative log marginal likelihood. Once these modifications have been made, uncertainty-equipped DeepONet models are trained using the same procedure as standard DeepONet models. In practice, some additional adjustments to the input data are sometimes required to prevent the training procedure from diverging at the start of training due to numerical overflow. For example, when using a normal distribution to model the network’s output, small variance predictions can lead to extremely large loss values (which can result in overflow and stall training completely). This can be avoided by rescaling input data so that the initial outputs of the networks are on a reasonable scale (e.g., on the order of -10 to 10 for log standard deviation predictions). This rescaling step is generally sufficient, and it was all that was required for the experiments in this work. For other applications, it is possible that training could destabilize later on in the training procedure due to excessively low variance predictions. In this case, clipping can be used to impose an absolute limit on the minimum variance value output by the network.

Appendix A.1. Network variants for boundary conditions and uncertainty quantification

One technical challenge associated with neural network approximations for PDEs is the incorporation of boundary conditions. Handling input data associated with inhomogeneous boundary conditions is complicated by the fact that the dimensionality of boundary data is strictly less than that of the interior data, as shown in Fig. 4. This leads to a sparse representation of the boundary data in the ambient space and poses a significant challenge for convolutional architectures in practice. For fully-connected layers, the boundary can simply be appended to the list of sensor values associated with the interior data. We conducted a series of ablation studies to determine the appropriate network architecture for handling inhomogeneous boundary conditions. The architecture illustrated at the top left of Fig. A.1 was ultimately chosen due to its simplicity; while the other two variations achieved similar performance, there was no observable benefit associated with separate processing components used for the interior data, $f \in C(\Omega)$, and boundary data, $g \in C(\partial\Omega)$.

Once the architecture for the inclusion of boundary conditions was selected, additional ablation experiments were conducted in order to identify the best network design regarding uncertainty predictions. We hypothesized that the performance of the uncertainty framework could be improved by decoupling the mean and standard deviation predictions during the final layers of the branch and trunk networks. This is motivated by the fact that the output of the trunk network serve as basis functions for the final model predictions. By separating the trunk at the end, it is possible for the network to learn a distinct set of basis functions for its uncertainty predictions (instead of relying on the basis functions learned for the mean predictions). We considered three architecture variations for decoupling the uncertainty predictions, which are shown in the right column of Fig. A.1. The first variant uses a shared trunk network while incorporating a split head in the branch network to decouple the mean and uncertainty predictions. This architecture consistently performed the worst among the three variants. The remaining architectures also decouple predictions in the trunk network, with the first doing so in the final layers of the network and the latter

incorporating an entirely separate network for trunk uncertainty predictions. We observed similar performance with both variants and elected to use the simpler architecture (shown in the center-right of Fig. A.1) since it requires less trainable parameters (and significantly less overhead) than the fully-decoupled alternative.

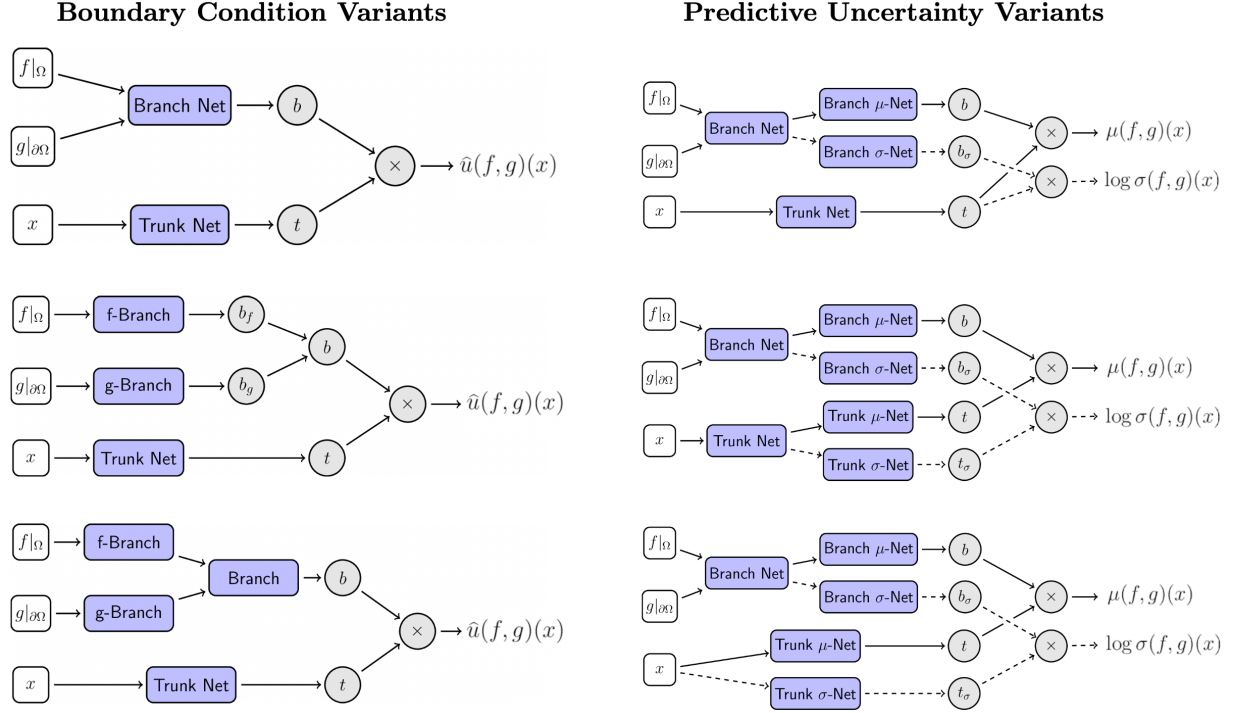


Figure A.1: DeepONet architecture variants for the incorporation of boundary conditions (left) and the prediction of uncertainty parameters (right). The simplest variant for handling boundary conditions (top-left) was found to match the performance of more structured architectures. For uncertainty-equipped operator networks, we found that decoupling the trunk predictions for mean and uncertainty parameters consistently improved the performance of the network. The second variant on the right was selected since it introduces far less trainable parameters than independent uncertainty networks and was observed to achieve similar levels of performance.

References

- [1] R. C. Smith, Uncertainty quantification: theory, implementation, and applications, Vol. 12, Siam, 2013.
- [2] T. J. Sullivan, Introduction to uncertainty quantification, Vol. 63, Springer, 2015.
- [3] G. E. Karniadakis, I. G. Kevrekidis, L. Lu, P. Perdikaris, S. Wang, L. Yang, Physics-informed machine learning, *Nature Reviews Physics* 3 (6) (2021) 422–440.
- [4] G. Cybenko, Approximation by superpositions of a sigmoidal function, *Mathematics of control, signals and systems* 2 (4) (1989) 303–314.
- [5] K. Hornik, M. Stinchcombe, H. White, Multilayer feedforward networks are universal approximators, *Neural networks* 2 (5) (1989) 359–366.
- [6] M. Leshno, V. Y. Lin, A. Pinkus, S. Schocken, Multilayer feedforward networks with a nonpolynomial activation function can approximate any function, *Neural networks* 6 (6) (1993) 861–867.
- [7] L. Lu, P. Jin, G. Pang, Z. Zhang, G. E. Karniadakis, Learning nonlinear operators via deeponet based on the universal approximation theorem of operators, *Nature Machine Intelligence* 3 (3) (2021) 218–229.
- [8] C. Lin, Z. Li, L. Lu, S. Cai, M. Maxey, G. E. Karniadakis, Operator learning for predicting multiscale bubble growth dynamics, *The Journal of Chemical Physics* 154 (10) (2021) 104118.
- [9] S. Cai, Z. Wang, L. Lu, T. A. Zaki, G. E. Karniadakis, Deepm&mnet: Inferring the electroconvection multi-physics fields based on operator approximation by neural networks, *Journal of Computational Physics* 436 (2021) 110296.
- [10] Z. Mao, L. Lu, O. Marxen, T. A. Zaki, G. E. Karniadakis, Deepm&mnet for hypersonics: Predicting the coupled flow and finite-rate chemistry behind a normal shock using neural-network approximation of operators, *arXiv preprint arXiv:2011.03349* (2020).
- [11] S. Wang, H. Wang, P. Perdikaris, Learning the solution operator of parametric partial differential equations with physics-informed deeponets, *arXiv preprint arXiv:2103.10974* (2021).
- [12] P. C. Di Leoni, L. Lu, C. Meneveau, G. Karniadakis, T. A. Zaki, Deeponet prediction of linear instability waves in high-speed boundary layers, *arXiv preprint arXiv:2105.08697* (2021).
- [13] M. Yin, E. Ban, B. V. Rego, E. Zhang, C. Cavinato, J. D. Humphrey, G. E. Karniadakis, Simulating progressive intramural damage leading to aortic dissection using an operator-regression neural network, *arXiv preprint arXiv:2108.11985* (2021).
- [14] S. Goswami, M. Yin, Y. Yu, G. Karniadakis, A physics-informed variational deeponet for predicting the crack path in brittle materials, *arXiv preprint arXiv:2108.06905* (2021).
- [15] S. Goswami, M. Yin, Y. Yu, G. E. Karniadakis, A physics-informed variational deeponet for predicting crack path in quasi-brittle materials, *Computer Methods in Applied Mechanics and Engineering* 391 (2022) 114587.
- [16] S. Goswami, K. Kontolati, M. D. Shields, G. E. Karniadakis, Deep transfer learning for partial differential equations under conditional shift with deeponet, *arXiv preprint arXiv:2204.09810* (2022).
- [17] S. Mao, R. Dong, L. Lu, K. M. Yi, S. Wang, P. Perdikaris, Ppdnet: Deep operator networks for fast prediction of steady-state solutions in disk–planet systems, *The Astrophysical Journal Letters* 950 (2) (2023) L12.
- [18] M. Zhu, S. Feng, Y. Lin, L. Lu, Fourier-deeponet: Fourier-enhanced deep operator networks for full waveform inversion with improved accuracy, generalizability, and robustness, *Computer Methods in Applied Mechanics and Engineering* 416 (2023) 116300.
- [19] Z. Jiang, M. Zhu, L. Lu, Fourier-mionet: Fourier-enhanced multiple-input neural operators for multiphase modeling of geological carbon sequestration, *Reliability Engineering & System Safety* 251 (2024) 110392.
- [20] J. E. Lee, M. Zhu, Z. Xi, K. Wang, Y. O. Yuan, L. Lu, Efficient and generalizable nested fourier-deeponet for three-dimensional geological carbon sequestration, *Engineering Applications of Computational Fluid Mechanics* 18 (2024) 2435457.

- [21] M. Zhu, H. Zhang, A. Jiao, G. E. Karniadakis, L. Lu, Reliable extrapolation of deep neural operators informed by physics or sparse observations, *Computer Methods in Applied Mechanics and Engineering* 412 (2023) 116064.
- [22] B. Deng, Y. Shin, L. Lu, Z. Zhang, G. E. Karniadakis, Approximation rates of deeponets for learning operators arising from advection-diffusion equations, *Neural Networks* 153 (2022) 411–426.
- [23] M. Yin, N. Charon, R. Brody, L. Lu, N. Trayanova, M. Maggioni, A scalable framework for learning the geometry-dependent solution operators of partial differential equations, *Nature Computational Science* 4 (2024) 928–940.
- [24] A. Jiao, Q. Yan, J. Harlim, L. Lu, Solving forward and inverse pde problems on unknown manifolds via physics-informed neural operators, *arXiv preprint:2407.05477* (2024).
- [25] P. Xiao, M. Zheng, X. Yang, L. Lu, Quantum deeponet: Neural operators accelerated by quantum computing, *arXiv preprint:2409.15683* (2024).
- [26] S. Mao, R. Dong, K. M. Yi, L. Lu, S. Wang, P. Perdikaris, Disk2planet: A robust and automated machine learning tool for parameter inference in disk–planet systems, *The Astrophysical Journal* 976 (2) (2024) 200.
- [27] G. Lin, C. Moya, Z. Zhang, B-deeponet: An enhanced bayesian deeponet for solving noisy parametric pdes using accelerated replica exchange sgld, *Journal of Computational Physics* (2022) 111713.
- [28] Y. Yang, G. Kissas, P. Perdikaris, Scalable uncertainty quantification for deep operator networks using randomized priors, *arXiv preprint arXiv:2203.03048* (2022).
- [29] C. Moya, S. Zhang, M. Yue, G. Lin, Deeponet-grid-ug: A trustworthy deep operator framework for predicting the power grid’s post-fault trajectories, *arXiv preprint arXiv:2202.07176* (2022).
- [30] C. Moya, A. Mollaali, Z. Zhang, L. Lu, G. Lin, Conformalized-deeponet: A distribution-free framework for uncertainty quantification in deep operator networks, *Physica D: Nonlinear Phenomena* 471 (2025) 134418.
- [31] E. Pickering, S. Guth, G. E. Karniadakis, T. P. Sapsis, Discovering and forecasting extreme events via active learning in neural operators, *Nature Computational Science* 2 (2022) 823–833.
- [32] B. Settles, Active learning literature survey, Tech. rep., University of Wisconsin-Madison Department of Computer Sciences (2009).
- [33] Y. Gal, R. Islam, Z. Ghahramani, Deep bayesian active learning with image data, in: *Proceedings of the 34th International Conference on Machine Learning-Volume 70, JMLR, 2017*, pp. 1183–1192.
- [34] N. Houthby, F. Huszár, Z. Ghahramani, M. Lengyel, Bayesian active learning for classification and preference learning, *arXiv preprint arXiv:1112.5745* (2011).
- [35] G. E. Karniadakis, I. G. Kevrekidis, L. Lu, P. Perdikaris, S. Wang, L. Yang, Physics-informed machine learning, *Nature Reviews Physics* 3 (2021) 422–440.
- [36] N. Winovich, K. Ramani, G. Lin, Convpede-ug: Convolutional neural networks with quantified uncertainty for heterogeneous elliptic partial differential equations on varied domains, *Journal of Computational Physics* 394 (2019) 263–279.
- [37] P. Jin, S. Meng, L. Lu, Mionet: Learning multiple-input operators via tensor product, *SIAM Journal on Scientific Computing* 44 (6) (2022) A3490–A3514.
- [38] L. Lu, X. Meng, S. Cai, Z. Mao, S. Goswami, Z. Zhang, G. E. Karniadakis, A comprehensive and fair comparison of two neural operators (with practical extensions) based on fair data, *Computer Methods in Applied Mechanics and Engineering* 393 (2022) 114778.
- [39] G. Strang, G. Fix, *An Analysis of the Finite Element Method*, Prentice-Hall Series in Electronic Technology, Prentice-Hall, 1973.
URL <https://books.google.com/books?id=VZRRAAAAAAAJ>
- [40] S. Larsson, V. Thomée, *Partial differential equations with numerical methods*, Vol. 45, Springer, 2003.

- [41] N. Winovich, Neural network approximations to solution operators for partial differential equations, Ph.D. thesis, Purdue University (2021).
- [42] A. L. Maas, A. Y. Hannun, A. Y. Ng, et al., Rectifier nonlinearities improve neural network acoustic models, in: Proc. icml, Vol. 30, Atlanta, GA, 2013, p. 3.
- [43] T. Chen, H. Chen, Universal approximation to nonlinear operators by neural networks with arbitrary activation functions and its application to dynamical systems, IEEE Transactions on Neural Networks 6 (4) (1995) 911–917. doi:10.1109/72.392253.
- [44] C. E. Rasmussen, Gaussian processes in machine learning, in: Summer school on machine learning, Springer, 2003, pp. 63–71.
- [45] D. Hendrycks, K. Gimpel, A baseline for detecting misclassified and out-of-distribution examples in neural networks, arXiv preprint arXiv:1610.02136 (2016).
- [46] R. B. Kline, Principles and practice of structural equation modeling, Guilford publications, 2023.
- [47] D. D. Cox, S. John, A statistical method for global optimization, in: [Proceedings] 1992 IEEE international conference on systems, man, and cybernetics, IEEE, 1992, pp. 1241–1246.